Capturing optoelectronic properties of $Cs_2AgSbBr_{6-x}Cl_x$ ($x = 0$–6) double perovskites using many-body perturbation theory

Surajit Adhikari [*] and Priya Johari [†]

Department of Physics, School of Natural Sciences, Shiv Nadar Institution of Eminence, Greater Noida, Gautam Buddha Nagar, Uttar Pradesh 201314, India

(Received 29 September 2023; revised 11 June 2024; accepted 13 June 2024; published 1 July 2024)

Lead-free inorganic $A_2M(\mathrm{I})M(\mathrm{III})X_6$ halide double perovskites (HDPs) are potentially benign materials with improved chemical stability as compared to organic lead halide perovskites. However, achieving comparable efficiency in optoelectronic devices requires careful exploration of suitable HDPs with favorable electronic, optical, and transport properties. In these efforts, we comprehensively studied $Cs_2AgSbBr_{6-x}Cl_x$ ($x = 0$–6) mixed HDPs by employing state-of-the-art first-principles-based density functional theory, density functional perturbation theory, and many-body perturbation theory, namely G_0W_0 and the Bethe-Salpeter equation (BSE). Our findings demonstrate the thermodynamic and mechanical stability of these materials. Furthermore, the structural polymorphs for $x = 2$, 3, and 4 exhibit nearly identical energies, indicating remarkably similar structural stability. The electronic band gap (indirect), calculated through HSE06 and G_0W_0, ranges from 1.68 to 2.49 eV. Meanwhile, the exciton binding energy, determined via standard BSE calculations, rises from 0.18 to 0.37 eV with increasing Cl concentration. The Fröhlich model is also used to account for the impact of electron (hole)–phonon coupling, and electron mobility is found to increase with a decrease in Cl concentration from 5.07 to 28.07 $cm^2\,V^{-1}\,s^{-1}$, while hole mobility shows an oscillating behavior. Overall, the meritorious tunable properties of mixed HDPs underscore their potential as stable, nontoxic materials with favorable attributes for optoelectronic applications.

DOI: 10.1103/PhysRevB.110.014101

I. INTRODUCTION

Lead halide perovskites have garnered significant interest in photovoltaic applications during the past decade due to their low manufacturing cost and exceptional optical and electronic properties, which include a suitable band gap [1,2], high optical absorption coefficient [3], long carrier diffusion length, low exciton binding energy [4,5], high carrier mobility [6], and high defect tolerance ability [7,8]. Due to these promising optoelectronic properties, both inorganic and organic-inorganic lead halide perovskites [$APbX_3$ ($A = Cs^+$, $CH_3NH_3^+$; $X = Cl^-$, Br^-, I^-)] are sought after for several applications, which include highly efficient solar cells [9,10], data storage, water splitting, light-emitting diodes (LEDs) [11], lasers, and photoelectric detectors with ultrahigh sensitivity and fast response [12,13]. In the past 10 years, lead halide perovskite–based solar cells' power conversion efficiency has risen from 3.8% to 26.1% [14,15]. It has been demonstrated that one efficient way to improve the properties of $CH_3NH_3PbX_3$ is to tune compositional components, particularly halogen ions. For instance, compared to $MAPbI_3$, $MAPbI_{3-x}Cl_x$ ($MA = CH_3NH_3^+$, $0 < x < 3$) have significantly longer electron-hole diffusion length [16]. Similarly, mixed halide perovskites, such as $MAPbI_{3-x}Br_x$ and $MAPbBr_{3-y}Cl_y$ crystals, have also been synthesized [17,18], and it has been shown that their band gap may be regulated nearly throughout the whole visible range by adjusting the ratio of the halide anions. In addition, mixed halide perovskites such as $MAPbI_{3-x}Cl_x$, $MAPbI_{3-x}Br_x$, and $MAPbBr_{3-x}Cl_x$ have been shown to exhibit improved charge carrier transport properties and a continuous band gap range, enabling them to be used in both single- and multiple-junction solar cells [19,20]. Due to this, throughout the past few years, the lead halide perovskites and their mixed halide family have received the most significant research attention for photovoltaics. However, despite their immense potential, they face two major bottlenecks that prevent them from being widely used, i.e., Pb toxicity and material instability [21]. The stability problems have been partially resolved by substituting an inorganic cesium ion for the organic cation [22,23]. Nonetheless, Pb toxicity still exists as a disadvantage, and it is crucial to address this problem without sacrificing effectiveness.

To resolve this issue, recently all-inorganic halide double perovskites $A_2M(\mathrm{I})M(\mathrm{III})X_6$ have been proposed as high-performance, lead-free, and stable potential materials for optoelectronic and solar cell applications [24–26]. These materials are created by swapping two toxic Pb^{2+} cations with a pair of nontoxic or less toxic heterovalent, i.e., monovalent and trivalent, metal cations. These halide double perovskites (HDPs) [$Cs_2M(\mathrm{I})M(\mathrm{III})X_6$ ($M(\mathrm{I}) = Ag^+$, Na^+; $M(\mathrm{III}) = Bi^{3+}$, In^{3+}, Sb^{3+}; $X = Cl^-$, Br^-)], in particular, have already been studied experimentally as well as computationally for a variety of device applications, including solar cells, LEDs, radiation detectors, and spintronics [27–32]. It has also been

[*]Contact author: sa731@snu.edu.in
[†]Contact author: priya.johari@snu.edu.in

shown that the optical and electronic properties of the HDPs can be changed significantly by adjusting the composition. Since the hybridization of metal [M(I), M(III)] and halide (X) orbitals plays a crucial role in defining the valence band maxima (VBMs) and conduction band minima (CBMs), the band gap (E_g) tuning can easily be attained by varying cationic or/and anionic configurations. In particular, cations contribute majorly to the CBMs, while anions primarily determine the character of the VBMs. Owing to a higher possibility for manipulation in anionic configuration, a larger band gap tunability can be achieved via blueshift of VBMs through anionic mixing as compared to the redshift of CBMs via cationic replacement [33–35].

Several experimental and theoretical studies are available for such HDPs that have focused on the cationic substitution for tuning the optoelectronic properties. For instance, experimentally mixed alloyed double perovskite compounds, such as $Cs_2AgBi_{1-x}M_xBr_6$ (M = In and Sb) [36] have been synthesized, characterized, and shown to exhibit tunable indirect (direct) band gap of from 1.86 (2.15) eV to 2.27 (2.41) eV. However, in theory $Cs_2AgSb_xBi_{1-x}Cl_6$ [34,37], $Cs_2Na_xAg_{1-x}BiCl_6$ [37], alloyed $Cs_2AgInCl_6$ [38] double perovskites, etc., have been studied and shown that band gaps lie in the range 2.37–3.77 eV. On the other hand, anionic mixing by considering different compositional combinations of halides have also been performed to modulate the optoelectronic properties of HDPs. For example, $Cs_2AgBiBr_{6-x}Cl_x$ [33,39,40] and $Cs_2AgBiBr_{6-x}I_x$ [41] double perovskites have been studied experimentally, while first-principles studies have been performed to investigate several lead-free mixed HDPs such as $Cs_2AgBiBr_{6-x}Cl_x$ [35,37], $Cs_2AgInBr_{6(1-x)}Cl_{6x}$ [42], and $Cs_2NaM(I_xBr_{1-x})_6$ (M = Bi, In) [43], and the tunability of optoelectronic properties has been demonstrated ($E_g \sim$ 2.39–4.47 eV) by varying the halide configuration.

We can infer from this literature that halide mixing is one of the best methods for modulating the band gap and broadening the spectral response, especially in the visible light region. Thus, by considering all-inorganic lead-free mixed HDPs, not only the problem of stability and environmental issues can be resolved, but there is also a possibility of achieving high efficiency via band gap modulation. According to the reports, the (direct or indirect) band gap of Cs_2AgBiX_6 (X = Br, Cl) [32,35], Cs_2AgInX_6 [29,44], Cs_2NaBiX_6 [43,45], Cs_2NaInX_6 [46,47], and Cs_2AgSbX_6 [27,28] compounds lie in the range 2.39–3.09 eV, 2.36–3.57 eV, 3.38–4.07 eV, 3.84–5.10 eV, and 1.64–2.61 eV, respectively. The selection of Cs in these compounds is driven by a balance between computational efficiency, favorable ionic size, stability considerations, and a limited impact on the electronic properties of interest. This choice facilitates both theoretical investigations and practical applications in the quest to understand and optimize the optoelectronic properties of these materials. As can be noticed, among the above mentioned HDPs, Cs_2AgSbX_6 (X = Br, Cl) have a desirable band gap range. Furthermore, these materials have been demonstrated to be stable in air, exhibiting lower exciton binding energy and long carrier recombination lifetime compared to neighboring compounds like Cs_2MSbX_6 (M = Na, K, Rb, Cs; X = Cl, Br), $Cs_2CuSbCl_6$, and $Cs_2AgInCl_6$ [26–29,38,48], desirable for enhancing the efficiency of optoelectronic devices. However, the mixed halide compounds $Cs_2AgSbBr_{6-x}Cl_x$ have not yet been studied.

To unlock the full potential of $Cs_2AgSbBr_{6-x}Cl_x$ compounds for photoelectric detection, it is crucial to establish a robust correlation between compositional configuration and optoelectronic properties. Moreover, it is also important to study the impact of anionic mixing in all-inorganic lead-free HDPs on their mechanical, transport, excitonic, and polaronic properties. Mechanical aspects, such as elastic modules, largely impact the flexibility, while the generation of excitons significantly influences the charge-separation properties in optoelectronic devices such as solar cells. Therefore, it is crucial to accurately estimate excitonic properties such as exciton binding energy, exciton radius, and exciton lifetime in these materials. Furthermore, the idea of polarons has also been used to explain a number of photophysical phenomena in HDP materials [38,49]. The dynamics of excitons and charge transport have been shown to be greatly influenced by the polaronic effects, as the carrier mobility depends on the strength of electron-phonon coupling, which has an impact on the separation of free charge carriers. Thus, it is crucial to comprehend the impact of electron-phonon coupling on polaron mobility, particularly in these mixed halide polar perovskites. To the best of our knowledge, despite several investigations on mixed halide double perovskites, a fundamental understanding of the excitonic and polaronic effects on such materials has not been achieved yet.

In this paper, we have therefore performed a systematic and comprehensive study of structural, mechanical, electronic, optical, transport, excitonic, and polaronic properties of $Cs_2AgSbBr_{6-x}Cl_x$ (x = 0, 1, 2, 3, 4, 5, 6) mixed halide double perovskites using density functional theory (DFT) [50,51] and state-of-the-art methods that go beyond DFT, i.e., many-body perturbation theory (MBPT) based GW and BSE [52–55]. First, we used a semilocal PBE exchange-correlation (xc) functional to optimize crystal structures and demonstrated that the cell volume grows linearly when the Br/Cl ratio increases. Then, to compute the electronic properties, we used the hybrid HSE06 [56] xc functional as well as MBPT-based GW [54,55] (G_0W_0@PBE) method. Following that, we ascertained the optical properties using the Bethe-Salpeter equation (BSE) [52,53] based calculations on top of the single-shot GW (G_0W_0)@PBE to obtain the electronic contribution to the dielectric function and the exciton binding energy. We predicted that these perovskites have a lower exciton binding energy value than their neighboring compounds like pristine and alloyed $Cs_2AgInCl_6$ [38] and $Cs_2AgBiBr_6$ [57], but have relatively higher values than lead halide perovskites, which leads to a trade-off between toxicity and efficiency. However, we firmly believe this bottleneck can be overcome by defect engineering or considering heterostructures. Furthermore, for the first time, this class of materials has undergone research on numerous significant aspects, including excitonic properties and the importance of electron-phonon coupling, and are shown to be promising. Finally, we discussed the impact of electron-phonon coupling and computed the polaron mobility using the Hellwarth model [58]. In light of this research, $Cs_2AgSbBr_{6-x}Cl_x$ appears to be a highly potential candidate for optoelectronic applications.

II. COMPUTATIONAL DETAILS

In this paper, the first-principles density functional theory (DFT) [50,51] and many-body perturbation theory (MBPT) based calculations were performed using the Vienna *Ab initio* Simulation Package (VASP) [59,60]. The interaction between the valence and core electrons was treated using projector-augmented wave (PAW) [61] pseudopotentials. The PAW pseudopotentials were considered with valence shell electronic configurations for Cs, Ag, Sb, Cl, and Br as $5s^2 5p^6 6s^1$, $4d^{10} 5s^1$, $5s^2 5p^3$, $3s^2 3p^5$, and $4s^2 4p^5$, respectively. The exchange-correlation (xc) functional of Perdew, Burke, and Ernzerhof (PBE), based on the generalized gradient approximation (GGA) [62], was used to account for the electron-electron interactions. The kinetic energy cutoff for plane-wave basis set expansion was set at 400 eV. The threshold for the electronic self-consistent-field iteration energy convergence was chosen as 10^{-6} eV. All structures were optimized using the PBE functional until Helmann-Feynman forces on each atom were less than 0.01 eV/Å. The Γ-centered $6 \times 6 \times 6$ **k**-point sampling was applied for Brillouin zone integration in order to determine the optimized structures. The crystal structures were drawn using Visualization for Electronic and STructural Analysis (VESTA) [63]. The band structures were estimated using the PBE xc functional, with the spin-orbit coupling (SOC) effect taken into account. Since PBE is known to underestimate the electronic properties, the electronic band gap was also calculated using the hybrid HSE06 [56] xc functional (exact exchange = 25%) and MBPT-based *GW* [54,55] (G_0W_0@PBE) method for more precise estimation. The Sumo [64] code was used to compute the effective mass. To determine the optical properties with accuracy, we performed Bethe-Salpeter equation (BSE) [52,53] calculations on top of the single-shot *GW* (G_0W_0)@PBE, which explicitly takes into account the electron-hole interaction. Note that a Γ-centered $4 \times 4 \times 4$ **k** grid and a converged NBANDS value of 540 were used for *GW*-BSE calculations, which were found accurate enough to predict the results up to the desired energy range. The electron-hole kernel for BSE calculations was created using 6 occupied and 6 unoccupied bands. On the other hand, to calculate the ionic contribution of the dielectric function, density functional perturbation theory (DFPT) [65] calculations were performed using a denser $6 \times 6 \times 6$ **k** grid for all the systems.

III. RESULTS AND DISCUSSION

In this study, to explore the potential of mixed halide $Cs_2AgSbBr_{6-x}Cl_x$ in view of efficient optoelectronic devices such as solar cells, photoelectric detectors, LEDs, etc., we conducted a thorough investigation to analyze the effect of halide mixing on the optoelectronic properties. In the following subsections, the stability as well as the structural, mechanical, electronic, optical, transport, excitonic, and polaronic properties of mixed $Cs_2AgSbBr_{6-x}Cl_x$ HDP are examined and discussed in detail to gain fundamental understanding and to direct future experimental studies.

A. Structural properties

1. Crystallographic stability

$A_2M(\mathrm{I})M(\mathrm{III})X_6$ stoichiometry describes the general crystallographic structure of a double perovskite material. Mainly, the crystallographic stability of perovskite materials has been estimated using two parameters: the Goldschmidt tolerance factor [66,67] (t) and the octahedral factor [67,68] (μ). Further, in a recent study, Bartel *et al.* proposed a new tolerance factor [69] (τ) to estimate the stability of halide perovskites. These three respective parameters are defined as follows [26]:

$$t = \frac{(r_A + r_X)}{\sqrt{2}\left[\frac{(r_{M(I)} + r_{M(III)})}{2} + r_X\right]}, \tag{1}$$

$$\mu = \frac{(r_{M(I)} + r_{M(III)})}{2r_X}, \tag{2}$$

$$\tau = \frac{2r_X}{(r_{M(I)} + r_{M(III)})} - n_A\left(n_A - \frac{2r_A/(r_{M(I)} + r_{M(III)})}{\ln[2r_A/(r_{M(I)} + r_{M(III)})]}\right), \tag{3}$$

where r_A, $r_{M(I)}$, $r_{M(III)}$, and r_X are the ionic radii for the respective ions, while n_A represents the oxidation state of the A-site cation [Eq. (3)] and $r_A > r_M$ by definition (r_M is the average ionic radius of $r_{M(I)}$ and $r_{M(III)}$ ions). In accordance with earlier research, stable 3D perovskite structures often form when μ and t values range between $0.442 < \mu < 0.895$ and $0.80 < t < 1.10$ [67,70], respectively, while as per Bartel *et al.*, $\tau < 4.18$ denotes a stable perovskite structure [69]. In this study, A is considered as Cs, M(I) and M(III) are the monovalent and trivalent metal cations, Ag and Sb, respectively, while the halide X is taken as Br or/and Cl. The halide ion radius (r_X) for $Cs_2AgSbBr_{6-x}Cl_x$ ($x = 0$–6) double perovskite has been evaluated as $r_X = [\{(6-x)r_{\mathrm{Br}} + xr_{\mathrm{Cl}}\}/6]$. For the $Cs_2AgSbBr_{6-x}Cl_x$ perovskites, the corresponding Shannon ionic radii of Cs^+, Ag^+, Sb^{3+}, Br^-, and Cl^- are considered as 1.88, 1.15, 0.76, 1.96, and 1.81 Å, respectively. As evident from Table I, the calculated t, μ, and τ values for $Cs_2AgSbBr_{6-x}Cl_x$ are in the ranges of 0.931–0.944, 0.487–0.528, and 3.802–3.959, respectively, essentially confirming them to be satisfying all crystallographic stability criteria. This reveals a high possibility for the formation of stable mixed halide $Cs_2AgSbBr_{6-x}Cl_x$ perovskites, where the parent compounds ($Cs_2AgSbBr_6$ and $Cs_2AgSbCl_6$) have already been shown to be synthesized successfully [27,28,30].

2. Crystal structure

The primitive crystal structure of halide double perovskite (HDP) $Cs_2AgSbBr_6$ is presented in Fig. 1. This schematic assigns an identification number (1–6) to each Br^- ion at different sites. Chloride ions gradually replace the bromide ions in $Cs_2AgSbBr_6$ HDP to form the mixed halide double perovskite $Cs_2AgSbBr_{6-x}Cl_x$. According to the experimental results and theoretical simulations, $Cs_2AgSbBr_6$ [28,71] and $Cs_2AgSbCl_6$ [27,30] structures both maintain the standard face-centered cubic (fcc) lattice with space group $Fm\bar{3}m$ (225). The Cs_2AgSbX_6 (X = Br, Cl) structure is composed of $[AgX_6]^{-5}$ and $[SbX_6]^{-3}$ regular octahedrons that are alternatively corner-shared to create a three-dimensional framework,

TABLE I. Optimized lattice parameters, space group, primary cell volume, Goldschmidt's tolerance factor (t), octahedral factor (μ), and new tolerance factor (τ) of mixed halide double perovskite $Cs_2AgSbBr_{6-x}Cl_x$ compounds.

System	Site of Cl-doped	Lattice parameters (Å) In this study	Lattice parameters (Å) Experimental value	Space group (No.)	Primary cell volume (Å^3)	t	μ	τ
$x = 0$		$a = b = c = 11.352$	$a = b = c = 11.184$ [71]	$Fm\bar{3}m$ (225)	365.70	0.931	0.487	3.959
$x = 1$	Br1	$a = b = 8.033$, $c = 11.105$		$I4mm$ (107)	358.32	0.933	0.494	3.933
$x = 2$ (para-Cl)	Br1, Br2	$a = b = 8.032$, $c = 10.860$		$I4/mmm$ (139)	350.29	0.935	0.500	3.906
$x = 2$ (ortho-Cl)	Br1, Br5	$a = 7.860$, $b = 11.354$, $c = 7.849$		$Imm2$ (44)	350.29	0.935	0.500	3.906
$x = 3$ (plane-Cl)	Br1, Br5, Br6	$a = 10.864$, $b = 11.335$, $c = 11.108$		$Fmm2$ (42)	341.97	0.937	0.507	3.879
$x = 3$ (RT-Cl)	Br1, Br3, Br5	$a = b = 7.848$, $c = 19.228$		$R3m$ (160)	341.85	0.937	0.507	3.879
$x = 4$ (para-Br)	Br3–6	$a = b = 7.696$, $c = 11.290$		$I4/mmm$ (139)	334.38	0.939	0.513	3.854
$x = 4$ (ortho-Br)	Br2, Br3, Br4, Br6	$a = 7.831$, $b = 10.896$, $c = 7.826$		$Imm2$ (44)	333.89	0.939	0.513	3.854
$x = 5$	Br2–6	$a = b = 7.683$, $c = 11.044$		$I4mm$ (107)	325.95	0.942	0.520	3.828
$x = 6$	Br1–6	$a = b = c = 10.836$	$a = b = c = 10.699$ [27]	$Fm\bar{3}m$ (225)	318.06	0.944	0.528	3.802

and the Cs^+ ion is situated in the middle of the framework cavities, resembling rocksalt ordering. The crystal structure of $Cs_2AgSbBr_{6-x}Cl_x$ ($x = 1, 5$) transforms to a body-centered tetragonal structure [space group $I4mm$ (107)] when one halide site is swapped out for the other, resulting in a decrease in structural symmetry. Similarly, when two halide sites are substituted for one another ($x = 2, 4$), the structure can either be tetragonal [space group $I4/mmm$ (139)] if the substitutes are situated in the "para" position (Br1 and Br2 sites), or orthorhombic [space group $Imm2$ (44)] if they are positioned in the "ortho" position (Br1 and Br5 sites). In contrast, for $x = 3$, the structure changes to a face-centered orthorhombic crystal [space group $Fmm2$ (42)] when the replacement X are in the same plane such that chloride (Cl^-) ions are doped in the Br1, Br5, and Br6 sites (plane-Cl). The structure deviates in the body's diagonal direction when X at the right angle positions (i.e., Br1, Br3, and Br5) are substituted by the other halide (Cl^-) type or vice versa (RT-Cl), resulting in a trigonal system [space group $R3m$ (160)]. This way, eight intermediate compositions are produced, where x can range from 1 to 5. These systems are simulated using their primitive cell, which consists of 10 atoms. The computed conventional crystal structures with 10 different configurations of $Cs_2AgSbBr_{6-x}Cl_x$ ($x = 0, 1, 2, 3, 4, 5, 6$) compounds are displayed in Fig. S1 of the Supplemental Material [72].

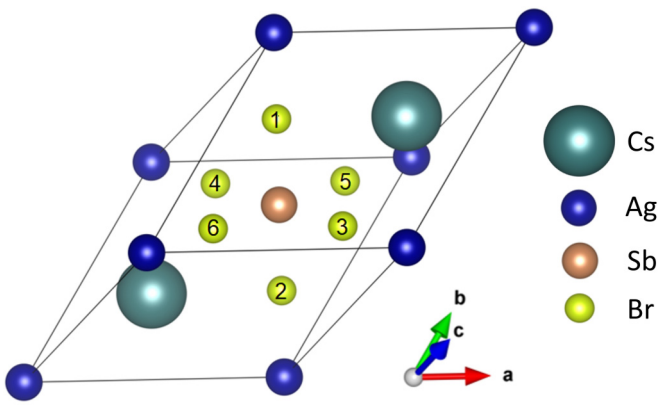

FIG. 1. Schematic figure of the primitive cell structure of halide double perovskite $Cs_2AgSbBr_6$.

Table I displays the optimized lattice constants, space group, and unit cell volume of the mixed halide double perovskite $Cs_2AgSbBr_{6-x}Cl_x$ ($x = 0, 1, 2, 3, 4, 5, 6$). With respect to $Cs_2AgSbBr_6$ ($a = 11.184$ Å [71]) and $Cs_2AgSbCl_6$ ($a = 10.699$ Å [27]), the computed lattice constant differs from the experimental value only by ~1.50% and 1.28%, respectively. It can be noticed that the primary cell volume of the mixed HDP decreases monotonically on going from Br to Cl. This happens due to the rise in the amount of the Cl^- ion, which has a smaller ionic radius and higher electronegativity than the Br^- ion. In the case of the Cs_2AgSbX_6 (X = Br, Cl) HDP structure, the Ag and Sb cations are octahedrally coordinated by the halide ions, and all of the Ag-X or Sb-X bond lengths are equivalent to each other. However, the regular octahedrons are distorted in the mixed HDPs, which led to a considerable change in the bond lengths and bond angles. In our study, the symmetry of the mixed HDPs changes due to the tilting of octahedra, whereas the different space groups reported in Table I result from element substitution within a primitive cell. Earlier diffraction experiments have shown that halide mixing preserves the elpasolite structure when the high-temperature cubic phase is maintained, with this preservation resulting from the statistical distribution of the replaced halide [41]. However, our results do not fully align with these experimental observations. The Ag-X and Sb-X (X = Br, Cl) bond lengths for all studied structures are tabulated in Table S2. It should be noted here that all the calculations are performed under ideal 0 K conditions. In principle, these compounds may experience some structural changes due to thermal expansion and dynamic motion at higher temperatures or room temperature, which may affect the electronic and optical properties of the materials. However, it is believed that the effect would not be substantial in qualitative terms and will not affect the trend in any way.

3. Thermodynamic stability

To examine the thermodynamic stability of the pure and mixed halide double perovskites, we first calculated their formation energy (E_f) by using the chemical equation [73–75]

$$E_f = E_{(Cs_2AgSbBr_{6-x}Cl_x)} - 2E_{Cs} - E_{Ag} - E_{Sb} - (6-x)E_{Br} - xE_{Cl}, \quad (4)$$

where $E_{(Cs_2AgSbBr_{6-x}Cl_x)}$ is the total energy of the host HDP material, $E_{Cs}/E_{Ag}/E_{Sb}/E_{Br}/E_{Cl}$ are the optimized energies of the respective atoms, and $x = 0, 1, 2, 3, 4, 5, 6$. The computed ground-state energies of Cs, Ag, Sb, Br, and Cl atoms are calculated to be −0.843 eV, −2.681 eV, −4.151 eV, −1.634 eV, and −1.840 eV, respectively. The formation energy is calculated using Eq. (4) for all structures and is listed in Table S2. It can be seen that all the investigated HDPs exhibit negative formation energy, indicating these materials to be energetically stable under certain thermodynamical conditions. It should also be noticed that replacing Br^- with Cl^- ions significantly reduces the formation energy and, thus, enhances the thermodynamic stability of Cl-rich compounds, owing to their larger electronegativity.

4. Mechanical stability and elastic properties

Subsequently, to ascertain the mechanical stability and elastic properties of these perovskites, we have calculated the second-order elastic constants (C_{ij}) of the materials using the energy-strain approach [76]. Since all of the HDPs considered in this study do not belong to the same class of crystal symmetry, there are various numbers of independent elastic constants. Three independent elastic constants (C_{11}, C_{44}, and C_{12}) for the cubic symmetry, six independent elastic constants (C_{11}, C_{33}, C_{44}, C_{66}, C_{12}, and C_{13}) for the tetragonal system, nine independent elastic constants ($C_{11}, C_{22}, C_{33}, C_{44}, C_{55}, C_{66}$, C_{12}, C_{13}, and C_{23}) for the orthorhombic symmetry, and only six independent elastic constants (C_{11}, C_{33}, C_{44}, C_{12}, C_{13}, and C_{14}) for the trigonal crystal system are necessary to explain the mechanical stability and related properties of the corresponding crystal system [76,77]. The calculated elastic constants for all HDPs are listed in Table S3, and the elastic constants for each system are found to satisfy the Born stability criteria [76,78], certifying the mechanical stability of the pure and mixed halide double perovskites.

Using the elastic constants tabulated in Table S3, the corresponding bulk modulus (B), shear modulus (G), Young's modulus (Y), and Poisson's ratio (ν) of these perovskites are calculated according to Voigt-Reuss-Hill approaches [77–79]. In our study, the large values of B compared to G indicate that the investigated HDPs exhibit better resistance to volumetric deformation than to shape deformation. On the other hand, lower values of G and Y show that these materials are less rigid and more flexible. In addition, Pugh's suggested B/G ratio [80] and Poisson's ratio (ν) are used to determine the fragility of these materials. The computed values of B/G (>1.75) and ν (>0.26) suggest that all considered double perovskites are ductile in nature. These specific mechanical properties make the considered HDPs appropriate for flexible and durable devices.

B. Electronic properties

To investigate the electronic properties of the considered HDPs, the total density of states (TDOS), the partial density of states (PDOS), the positions of the band edges, i.e., the valence band maxima (VBMs) and the conduction band minima (CBMs), and also the nature of the band gap are examined.

The electronic band structure of the primitive cell of $Cs_2AgSbBr_{6-x}Cl_x$ ($x = 0$ and $x = 6$) calculated using the PBE/PBE-SOC, HSE06 [56] xc functionals, and MBPT-based GW [54,55] (G_0W_0@PBE) method are depicted in Fig. 2, while the HSE06 calculated band structures for the mixed halides (x = 1–5) are shown in Fig. 3. It can be seen that irrespective of the functional, the VBMs and CBMs for $Cs_2AgSbBr_{6-x}Cl_x$ are found to be localized at different k points of the Brillouin zone, which makes them indirect band gap materials. The calculated value of the band gap of these compounds using the PBE/PBE-SOC, HSE06 xc functionals, and G_0W_0@PBE method are tabulated in Table II. Also, the position and value of the lowest direct band gap (E_g^{dir}) of these compounds are given in Table S6 and Table II, respectively. As per Fig. 2 and Table II, the PBE estimated band gap is lower than the HSE06 and G_0W_0@PBE calculated ones. Further, the band gap is not found to be much affected by the inclusion of spin-orbit coupling (SOC) effects with PBE (PBE-SOC). The energy band gap of $Cs_2AgSbBr_{6-x}Cl_x$ calculated using the HSE06 and G_0W_0@PBE methods are found to be in the range of 1.68–2.34 eV and 1.73–2.49 eV, respectively. The experimental indirect band gap of $Cs_2AgSbBr_6$ is 1.64 eV [28], which agrees well with the HSE06 calculated band gap (1.68 eV). On the other hand, the experimental band gap value for $Cs_2AgSbCl_6$ lies in between 2.54–2.61 eV [27,29,31,48], which is in good agreement with the band gap calculated using the G_0W_0@PBE method (2.49 eV). This reveals that the HSE06 or G_0W_0@PBE calculated band gap agrees well with the experimental values as compared to the PBE calculated band gap, as expected. The possible reasons for the difference between G_0W_0 calculations and experimental band gaps could arise from various factors, including the approximations inherent in theoretical methods, neglect of certain electron correlations, and limitations of the chosen exchange-correlation functionals as a starting point. Additionally, experimental factors like sample impurities, defects, environmental conditions, and variations in measurement techniques may also contribute to these deviations. In general, all $Cs_2AgSbBr_{6-x}Cl_x$ mixed halide double perovskites are indirect band gap materials, in which the band gap increases on going from Br to Cl, similarly to the case of the Pb halide perovskite but with a sharper slope, which implies a broader tunable energy range. The variation of band gap with respect to x is plotted in Fig. 4 and fitted for different functionals. The band gap increases linearly when x goes from 0 to 6, with a slope of around 0.1 eV. This trend is valid for all functionals with a small deviation of 89, 115, and 129 meV for the PBE, HSE06, and G_0W_0@PBE method, respectively. These relations may help in predicting the band gap of $Cs_2AgSbBr_{6-x}Cl_x$ where x is not an integer, which is common in the case of synthesis of these materials.

The computed TDOS and PDOS of the $Cs_2AgSbBr_{6-x}Cl_x$ mixed HDPs are shown in Figs. 3(i)–3(l) and Fig. S3 of the

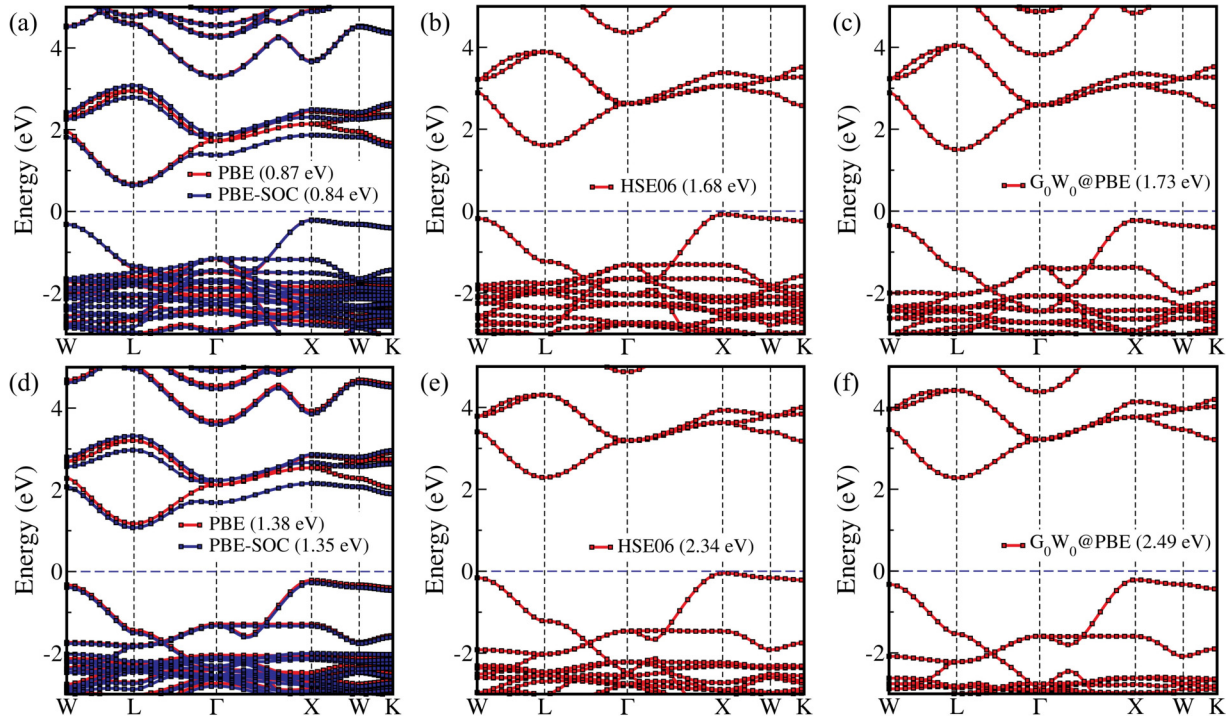

FIG. 2. Calculated band structures of [(a)–(c)] $Cs_2AgSbBr_6$ ($x = 0$) and [(d)–(f)] $Cs_2AgSbCl_6$ ($x = 6$) using the PBE/PBE-SOC, HSE06, and G_0W_0@PBE method, respectively. The Fermi level is set at zero and marked by the dashed blue line.

Supplemental Material [72]. From Figs. 3(i) and 3(l), it can be noticed that the VBM of $Cs_2AgSbBr_6$/$Cs_2AgSbCl_6$ mainly comprises Ag-4d and Br-4p/Cl-3p orbitals with dominance of the latter, while the CBM results from the hybridization of Ag-5s, Sb-5p, and Br-4p/Cl-3p states. In mixed HDPs, the contribution of both the halides can be witnessed as per their ratio, in VBMs and CBMs [Figs. 3(j) and 3(k)]. Consequently, the hybridization in the conduction band reduces with the increase in Cl concentration [owing to the change in cation-anion bond length (Table S2) and increase in the halogen's covalent nature (see Table S4)], which leads to the blueshift of the conduction band, and thus, an increase in the band gap on going from $Cs_2AgSbBr_6$ to $Cs_2AgSbCl_6$. Since the band gap of the examined HDPs is calculated in between ∼1.65–2.50 eV, covering a wide range of visible spectrum, they can prove to be promising materials for optoelectronic devices.

Further, the effective mass of the charge carriers for $Cs_2AgSbBr_{6-x}Cl_x$ compounds is also calculated as it is one of the crucial factors in determining the photogenerated carrier transport property [81] and is tabulated in Table III (for details, see the Supplemental Material [72]). The data clearly reveal that the electron effective mass of pure HDPs is smaller than their hole counterpart. On the contrary, in the mixed HDPs, the electron effective mass is mostly higher than the hole effective mass. These results suggest a tunability in the charge carrier mobility with respect to the mixing in the anionic configuration.

TABLE II. Computed band gap (E_g) and direct band gap (E_g^{dir}) of $Cs_2AgSbBr_{6-x}Cl_x$ compounds using the PBE/PBE-SOC, HSE06, and G_0W_0@PBE method.

	E_g (eV)				E_g^{dir} (eV)		
Configurations	PBE/PBE-SOC	HSE06	G_0W_0@PBE	Experimental	PBE/PBE-SOC	HSE06	G_0W_0@PBE
$x = 0$	0.87/0.84	1.68	1.73	1.64 [28]	1.90/1.85	2.71	2.80
$x = 1$	0.99/0.96	1.82	1.90		1.98/1.90	2.85	2.97
$x = 2$ (para-Cl)	1.05/1.02	1.87	1.98		2.04/2.00	2.90	3.04
$x = 2$ (ortho-Cl)	1.15/1.15	1.99	2.14		2.04/2.05	3.01	3.15
$x = 3$ (plane-Cl)	1.07/1.04	1.93	2.02		2.19/2.11	2.94	3.09
$x = 3$ (RT-Cl)	1.13/1.10	2.01	2.13		2.12/2.04	3.02	3.19
$x = 4$ (para-Br)	1.28/1.25	2.17	2.28		2.18/2.13	3.18	3.34
$x = 4$ (ortho-Br)	1.27/1.23	2.16	2.27		2.18/2.12	3.17	3.33
$x = 5$	1.36/1.33	2.29	2.41		2.27/2.19	3.28	3.47
$x = 6$	1.38/1.35	2.34	2.49	2.54–2.61 [27,29,31,48]	2.36/2.31	3.33	3.55

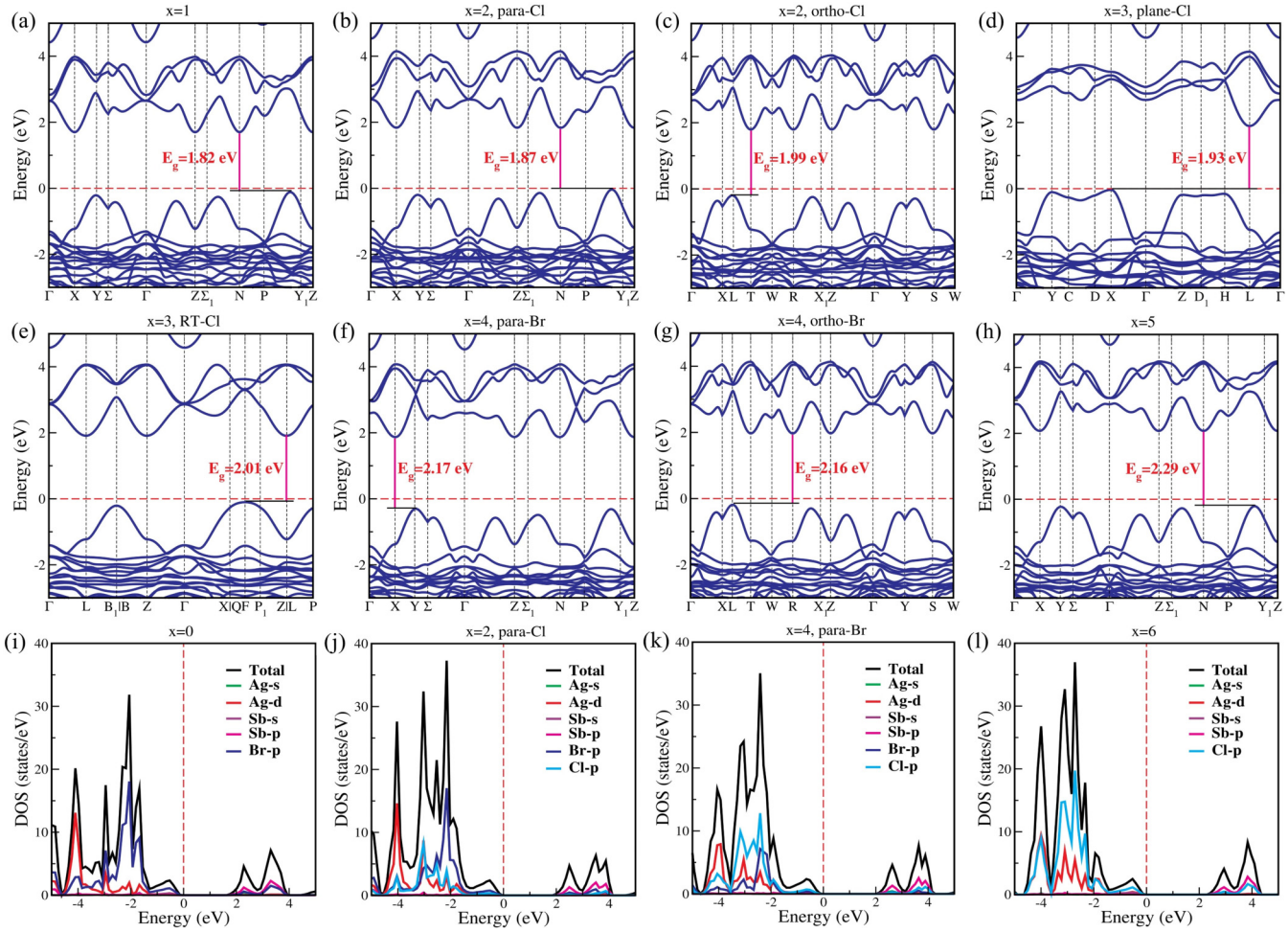

FIG. 3. [(a)–(h)] Calculated band structures of the $Cs_2AgSbBr_{6-x}Cl_x$ ($x = 1$, 2, 3, 4, and 5) compounds and [(i)–(l)] TDOS and PDOS of the $Cs_2AgSbBr_{6-x}Cl_x$ ($x = 0$, 2, 4, and 6) compounds using the HSE06 xc functional. The Fermi level is set to be zero and marked by the red line.

C. Optical properties

The tunable band gap in the wide range of the visible spectrum and low to moderate effective mass hint at $Cs_2AgSbBr_{6-x}Cl_x$ being promising materials for optoelectronic devices. Therefore, in this section, the suitability of the $Cs_2AgSbBr_{6-x}Cl_x$ mixed HDPs for efficient optoelectronic devices is evaluated by analyzing their optical properties, such as absorption coefficient and dielectric function. The optical absorption coefficient calculated using PBE and HSE06 xc functionals is presented in Fig. S4 of the Supplemental

TABLE III. Carrier's effective mass and dielectric constant of $Cs_2AgSbBr_{6-x}Cl_x$ compounds. Here, m_e^* represents electron effective mass, m_h^* represents hole effective mass, and μ^* represents reduced mass of charge carriers where m_0 is the rest mass of the electron, ε_∞ is the static electronic dielectric constant, and ε_{static} is the static ionic dielectric constant.

$Cs_2AgSbBr_{6-x}Cl_x$ configuration	m_e^* (m_0)	m_h^* (m_0)	μ^* (m_0)	ε_∞	ε_{static}
$x = 0$	0.272	0.377	0.158	3.36	11.08
$x = 1$	0.291	0.254	0.136	3.18	11.18
$x = 2$ (para-Cl)	0.308	0.232	0.132	3.04	11.88
$x = 2$ (ortho-Cl)	0.303	0.305	0.152	3.03	11.16
$x = 3$ (plane-Cl)	0.332	0.378	0.177	2.92	13.28
$x = 3$ (RT-Cl)	0.309	0.989	0.235	2.90	10.99
$x = 4$ (para-Br)	0.341	0.294	0.158	2.81	12.28
$x = 4$ (ortho-Br)	0.332	0.221	0.133	2.79	12.73
$x = 5$	0.346	0.299	0.160	2.65	11.93
$x = 6$	0.355	0.440	0.196	2.11	10.70

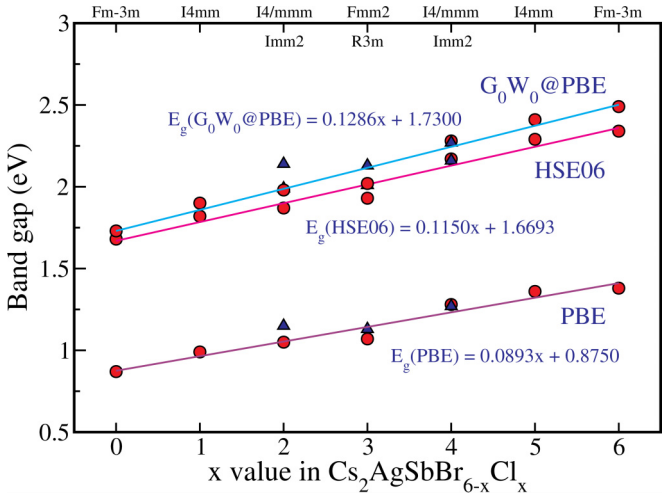

FIG. 4. Variation of the calculated band gap with the value of x in $Cs_2AgSbBr_{6-x}Cl_x$ compounds.

Material [72]. The optical absorption coefficient $\alpha(\omega)$ is computed considering the following expression [65,82],

$$\alpha(\omega) = \sqrt{2}\omega[\sqrt{[\mathrm{Re}(\varepsilon)]^2 + [\mathrm{Im}(\varepsilon)]^2} - \mathrm{Re}(\varepsilon)]^{1/2}, \quad (5)$$

where $\mathrm{Re}(\varepsilon)$ and $\mathrm{Im}(\varepsilon)$ are the real and imaginary part of the frequency-dependent dielectric constant, respectively. The optical properties of HDPs are known to be underestimated by the PBE functional due to the self-interaction error. On the other hand, the hybrid HSE06 xc functional has been shown to well describe the electronic properties of these materials, but less adept in foretelling the optical characteristics precisely [83]. Thus, here the optical response is also computed using a quite expensive but relatively more accurate MBPT-based BSE@G_0W_0@PBE [52,53] approach, which specifically takes into account the electron-hole interactions [84]. The optimized wave functions are considered as the starting point of the single-shot GW (G_0W_0)-BSE calculations. The absorption spectrum calculated using the PBE, HSE06, and BSE@G_0W_0@PBE methods for $Cs_2AgSbBr_6$ and $Cs_2AgSbCl_6$ are presented in Fig. 5. The calculations predict an optical gap of 1.95/2.76/2.38 eV (2.40/3.34/2.97 eV) for $Cs_2AgSbBr_6$ ($Cs_2AgSbCl_6$) using PBE/HSE06/BSE@G_0W_0@PBE, respectively. Rodrigues *et al.* [30] measured an optical gap of 2.70 eV for $Cs_2AgSbCl_6$ using the UV-vis spectrum. None of our results are in exact agreement with the experimental value; however, BSE@G_0W_0@PBE is found to give better agreement as compared to PBE and HSE06 xc functionals.

The averages of the optical responses, i.e., real and imaginary part of the dielectric function along the x, y, and z directions of $Cs_2AgSbBr_{6-x}Cl_x$ obtained using the BSE@G_0W_0@PBE method, are given in Figs. S8(a)–S8(j), while, the directional dielectric functions are presented in Fig. S7 of the Supplemental Material [72]. It can be seen from Fig. S7 that all the directional components approximately overlap each other, reflecting minimal anisotropy in the dielectric constant. Our findings (Fig. S8) reveal that the initial peak position of $Cs_2AgSbBr_{6-x}Cl_x$ compounds gets blueshifted with an increase in Cl concentration, which is consistent with the results of the electronic band gap. It should be noted here that the low energy absorption peaks lie in the mid-visible to near-UV region, and they can be tuned by varying the concentration of halides in the mixed HDPs.

The static electronic dielectric constant (also known as the dielectric function for zero photon energy) is a crucial parameter for optoelectronic applications because a high static dielectric constant results in a relatively low charge carrier recombination rate, which enhances the performance of optoelectronic devices [85]. Thus, in order to evaluate the efficiency of considered materials, static electronic dielectric constants (ε_∞) are also calculated using the BSE method and are tabulated in Table III. It can be seen that ε_∞ decreases with the increase in x and changes from 3.36 to 2.11 on going from $x = 0$ to 6, respectively. The decrease in ε_∞ indicates an increase in excitonic parameters such as exciton binding energy and excitonic temperature [38,86].

The intercept value along the energy axis in a plot between the imaginary part of the frequency-dependent dielectric function and the energy can be used to determine the absorption

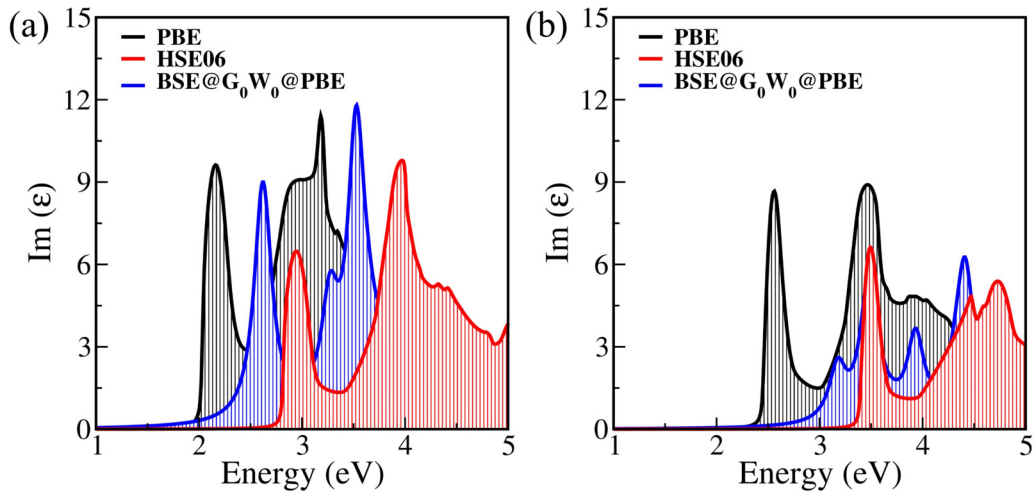

FIG. 5. Imaginary [$\mathrm{Im}(\varepsilon)$] part of the dielectric function for (a) $Cs_2AgSbBr_6$ and (b) $Cs_2AgSbCl_6$, obtained using PBE, HSE06, and BSE@G_0W_0@PBE method.

TABLE IV. Excitonic parameters for $Cs_2AgSbBr_{6-x}Cl_x$ compounds. Here, E_{exc} represents the exciton energy (in unit eV), E_B represents the exciton binding energy (in unit eV), T_{exc} represents the excitonic temperature (in unit K), μ^*_{exc} is the reduced mass of the exciton (in terms of rest mass of electron m_0), r_{exc} is the exciton radius (in unit nm), and $|\phi_n(0)|^2$ is the probability of a wave function at zero charge separation (in unit m^{-3}).

$Cs_2AgSbBr_{6-x}Cl_x$ configuration	E_{exc} (eV)	E_B (eV)	T_{exc} (K)	μ^*_{exc} (m_0)	r_{exc} (nm)	$\lvert\phi_n(0)\rvert^2$ (10^{27} m^{-3})
$x = 0$	2.62	0.18	2087	0.126	1.41	0.11
$x = 1$	2.71	0.26	3014	0.163	1.03	0.29
$x = 2$ (para-Cl)	2.78	0.26	3014	0.152	1.06	0.27
$x = 2$ (ortho-Cl)	2.80	0.35	4058	0.209	0.77	0.71
$x = 3$ (plane-Cl)	2.89	0.20	2319	0.106	1.46	0.10
$x = 3$ (RT-Cl)	2.91	0.28	3246	0.187	0.82	0.58
$x = 4$ (para-Br)	2.97	0.37	4290	0.202	0.74	0.80
$x = 4$ (ortho-Br)	3.00	0.33	3826	0.162	0.91	0.42
$x = 5$	3.11	0.36	4174	0.160	0.88	0.47
$x = 6$	3.18	0.37	4290	0.141	0.79	0.64

edge of $Cs_2AgSbBr_{6-x}Cl_x$ compounds. The absorption edge values calculated using PBE, HSE06, and BSE@G_0W_0@PBE are presented in Figs. S4 and S8. The PBE (HSE06) calculated absorption edge values lie in the range of 1.95–2.40 eV (2.76–3.34 eV), while the absorption edge values calculated using the BSE@G_0W_0@PBE method are in the range of 2.38–2.97 eV, indicating visible region light absorption by all the functionals/methods. Irrespective of the functional or approach, a monotonic increase in the absorption edge (optical band gap) is noticed with the rise in Cl concentration. Further, the calculated value of the absorption edge is compared with other results in the literature. For example, Su *et al.* [35] estimated the absorption edge to lie for $Cs_2AgBiBr_{6-x}Cl_x$ HDPs in the range of 2.38–2.75 eV (3.22–3.80 eV) using the PBE (HSE06) xc functional, which are much higher than our calculated values for $Cs_2AgSbBr_{6-x}Cl_x$ HDPs. The absorption edge for the similar mixed HDPs such as $Cs_2AgInBr_{6(1-x)}Cl_{6x}$ [42] and $Cs_2NaM(I_xBr_{1-x})_6$ (M = Bi, In) [43] are also predicted to be highly blueshifted as compared to our investigated systems. Further, as per HSE06 results, all investigated systems exhibit a large absorption coefficient ($\sim 10^5$ cm^{-1}), which denotes high-intensity optical transitions at the band edge (see Fig. S4 of the Supplemental Material [72]).

Overall, the versatile, tunable characteristics of mixed HDPs strongly indicate their potential as a valuable category of materials for various optoelectronic devices. This includes but is not limited to photodetectors, and green and blue LEDs to UV LEDs. Due to the high optical gap and low static dielectric constant, they might not be suitable for single solar cells as compared to their Pb counterpart but possibly be utilized in tandem solar cells if their band gap can be further adjusted through methods such as doping or the introduction of defects/vacancies. Exploration in this area is a forthcoming research endeavor that warrants attention in the future.

D. Excitonic properties

The exciton binding energy, another crucial variable in photovoltaic applications, is defined as the energy needed to dissociate the exciton into a single electron (e) and hole (h) pair. Theoretically, the difference between the energies of the bounded e-h pair (i.e., the BSE peak position) and unbounded noninteracting e-h pair (i.e., G_0W_0 direct band gap) is used to compute the exciton binding energy (E_B) [38,86–88]. In the Bethe-Salpeter equation (BSE) method, the e-h pair is bounded by the screened Coulomb interaction and the lowest peak position energy is referred as the exciton energy (E_{exc}) [38,87]. By knowing the exciton energy (E_{exc}) calculated using the BSE@G_0W_0@PBE method and G_0W_0@PBE direct band gap (E_g^{dir}), one can estimate the exciton binding energy (E_B) for indirect band gap materials [26,87,88] using the relation $E_B = E_g^{dir} – E_{exc}$. For the facile dissociation of exciton to create free charge carriers, a low E_B value is desirable. The calculated exciton energy (E_{exc}) and exciton binding energy (E_B) for a primitive cell of $Cs_2AgSbBr_{6-x}Cl_x$ mixed HDPs using the BSE@G_0W_0@PBE method are summarized in Table IV. Our results show that exciton binding energy values for the investigated mixed HDPs vary from 0.18 to 0.37 eV with no particular trend with respect to halide concentration. The calculated E_B for $Cs_2AgSbBr_6$ (0.18 eV) and $Cs_2AgSbCl_6$ (0.37 eV) are found close to but lower than the value reported by Biega *et al.* (0.25 eV and 0.43 eV, respectively) [89] using the BSE@G_0W_0@LDA method. The value for $Cs_2AgSbBr_6$ is also found to be lower than the experimental value of its neighboring compound $Cs_2AgBiBr_6$ (0.27 eV) [57], but slightly higher than the value calculated using the BSE@G_0W_0@LDA method for $Cs_2AgBiBr_6$ (0.17 eV) [89]. This difference may be explained due to precalculations done by Biega *et al.* at the LDA level. Further, the calculated E_B values for our investigated $Cs_2AgSbBr_{6-x}Cl_x$ compounds are found to be much lower than pristine and alloyed $Cs_2AgInCl_6$ double perovskites ($E_B \sim 0.58$–0.87 eV) [38]. However, the exciton binding energies for our investigated systems are lower than their neighboring compounds but are much higher ($\sim$5 times) than the lead halide perovskites. The higher values can be explained by the relatively flat dispersion at VBM for direct transition, which results in large effective masses and large E_B values (Fig. 2), quite similar to the case of transition metal dichalcogenides like MoS_2 and WS_2 [90]. However, by considering heterostructures to affect Coulomb screening in the barrier or by introducing defects/vacancies, a low binding energy may be achieved.

Following the determination of E_B, one can compute several additional excitonic parameters [84,91,92], including

excitonic temperature (T_{exc}), exciton radius (r_{exc}), and the probability of a wave function ($|\phi_n(0)|^2$) for the electron-hole pair at zero charge separation, which also play important roles in describing the efficiency of optoelectronic devices. The calculated value of these parameters is given in Table IV. One should notice that these parameters follow a similar trend as described for other perovskites [38,86]. Excitonic temperature is the maximum temperature at which an exciton will remain stable, and the thermal energy required to separate an exciton is $E_B = k_B T_{\text{exc}}$, where k_B is the Boltzmann constant. For example, $E_B = 0.20$ eV for $Cs_2AgSbBr_3Cl_3$ (plane-Cl), and therefore, excitons will be unstable above $T_{\text{exc}} = 2319$ K.

Next, the exciton radius (r_{exc}) [84,91,92] is calculated as follows:

$$r_{\text{exc}} = \frac{m_0}{\mu^*_{\text{exc}}} \varepsilon_{\text{eff}} n^2 r_{Ry}. \tag{6}$$

Here, m_0 is the rest mass of the electron, ε_{eff} is the effective dielectric constant, n is the exciton energy level ($n = 1$ provides the smallest exciton radius), $r_{Ry} = 0.0529$ nm is the Bohr radius, and μ^*_{exc} is the reduced mass of the exciton. In our study, $E_B \gg \hbar\omega_{LO}$, where ω_{LO} is the longitudinal optical phonon frequency, and therefore, $\varepsilon_{\text{eff}} \to \varepsilon_\infty$, showing the static value of the dielectric constant primarily consists of electronic contribution at a high frequency (ε_∞) [93,94]. The static electronic dielectric constant (ε_∞) is deduced from the real part of the dielectric function determined using the BSE@G_0W_0@PBE method (see Table III and Fig. S8). The reduced mass of the exciton (μ^*_{exc}) for $Cs_2AgSbBr_{6-x}Cl_x$ compounds is calculated at the point of direct band edges for every compound and found to increase when the Cl concentration increases, i.e., x goes from 0 to 2 in $Cs_2AgSbBr_{6-x}Cl_x$, while on a further increase of x, it is found to decrease.

The average separation between an electron (e) and a hole (h) within an exciton—which is a bound state of the e-h pair in a material—is referred to as the exciton radius (r_{exc}). Hence, a large exciton radius results in low charge carrier recombination rates and longer exciton lifetime (τ_{exc}). The calculated values of r_{exc} for our investigated HDPs are found to be higher than pristine and alloyed $Cs_2AgInCl_6$ HDPs ($r_{\text{exc}} \sim 0.47$–0.59 nm) [38], indicating a higher exciton lifetime for Cs_2AgSb-based mixed halide perovskites as compared to Cs_2AgIn-based halide perovskites.

The probability of a wave function ($|\phi_n(0)|^2$) for the e-h pair at zero charge separation is inversely related to the exciton radius (r_{exc}), which is determined using the exciton radius as follows [92]:

$$|\phi_n(0)|^2 = \frac{1}{\pi (r_{\text{exc}})^3 n^3}. \tag{7}$$

Using the value of $|\phi_n(0)|^2$, one can also calculate the intrinsic (or radiative) exciton lifetime (τ_{exc}) because τ_{exc} is inversely proportional to the $|\phi_n(0)|^2$ (for further details, see the Supplemental Material [72]). Accordingly, the $Cs_2AgSbBr_3Cl_3$ (plane-Cl) compound would have a longer intrinsic exciton lifetime, and $Cs_2AgSbBr_2Cl_4$ (para-Br) should have a shorter intrinsic exciton lifetime than the rest of the compounds (Table IV). The lower carrier recombination rate, which is indicated by the longer intrinsic exciton lifetime, leads to a better quantum yield and conversion efficiency. The longer intrinsic exciton lifetimes of the examined $Cs_2AgSbBr_{6-x}Cl_x$ compounds suggest that they are appropriate for use in photoelectric applications.

E. Polaronic properties

According to prototypical band theory, lead halide perovskites, such as $APbX_3$ ($A = Cs^+$, $CH_3NH_3^+$; $X = Cl^-$, Br^-, I^-) exhibit charge carrier mobility of the order of $\sim 10^3$ cm^2 V^{-1} s^{-1} [95,96], while experimental values have been reported in the range of 10–100 cm^2 V^{-1} s^{-1} [95,97]. It is found that Fröhlich's polaron model is a noteworthy model for explaining this discrepancy in mobilities between theory and experiments [38,95]. The model basically explains the effect of electron-phonon coupling on a material's physical characteristics and defines the dominant scattering process in polar semiconductors (such as halide perovskites) at room temperature as the interaction of carriers with the macroscopic electric field created by longitudinal optical (LO) phonons. Such interactions are known as the Fröhlich interactions [97–99]. Based on this model, the electron/hole mobilities are found to be in the range of 40–200 cm^2 V^{-1} s^{-1}, which are close to the experimental values [95].

In Fröhlich's polaron model, the polar optical phonons and the electron travelling through the lattice interact via the dimensionless Fröhlich parameter α, given as [38]

$$\alpha = \frac{1}{4\pi\varepsilon_0}\frac{1}{2}\left(\frac{1}{\varepsilon_\infty} - \frac{1}{\varepsilon_{\text{static}}}\right)\frac{e^2}{\hbar\omega_{LO}}\left(\frac{2m^*\omega_{LO}}{\hbar}\right)^{1/2}, \tag{8}$$

where ε_∞ and $\varepsilon_{\text{static}}$ are the static electronic and ionic dielectric constants, ε_0 is the permittivity of free space, m^* is the carrier effective mass, and ω_{LO} is the characteristic phonon angular frequency. For a system with multiple phonon branches, the average LO frequency is determined by taking the spectral average of all the infrared active optical phonon branches [58] (for further details, see the Supplemental Material [72]), and these LO frequencies are calculated using the DFPT method.

The values of α corresponding to electrons and holes for $Cs_2AgSbBr_{6-x}Cl_x$ perovskite compounds, which lie in between 3.84 to 8.38, are listed in Table V. In general, the value of $\alpha \ll 1$, indicates weak electron (hole)–phonon coupling, while strong coupling happens when $\alpha > 10$ [98]. This suggests that our systems of interest have an intermediate electron (hole)–phonon coupling. It can also be seen that the Fröhlich scattering strength in $Cs_2AgSbBr_{6-x}Cl_x$ increases as the high-frequency dielectric constant reduces. Further, as known, the lower Debye temperature (θ_D) as compared to the room temperature significantly increases electron (hole)–phonon interaction, and since the calculated Debye temperature (θ_D) for $Cs_2AgSbBr_{6-x}Cl_x$ compounds is significantly lower than room temperature, a significant polaronic contribution limiting the charge carrier mobility around room temperature should be expected. To verify that, in this work, we calculated the electron-phonon coupling associated charge carrier mobilities for $Cs_2AgSbBr_{6-x}Cl_x$.

We also estimated the specific free volume of $Cs_2AgSbBr_{6-x}Cl_x$ compounds to gain a qualitative understanding of the strength of electron-phonon coupling (for further details, see the Supplemental Material [72]). The difference between the volume of a unit cell and the

TABLE V. Polaron parameters corresponding to electrons (e) and holes (h) in $Cs_2AgSbBr_{6-x}Cl_x$ compounds. Here, ω_{LO} represents the characteristic phonon angular frequency (in unit THz), θ_D represents Debye temperature (in unit K), α represents Fröhlich interaction parameter, m_p represents effective mass of the polaron (in terms of m^*), and μ_p represents the polaron mobility (in unit $cm^2\,V^{-1}\,s^{-1}$).

			α		m_p/m^*		μ_p ($cm^2\,V^{-1}\,s^{-1}$)	
Configurations	ω_{LO} (THz)	θ_D (K)	e	h	e	h	e	h
$x = 0$	2.60	125	3.84	4.53	2.01	2.27	28.07	15.41
$x = 1$	2.67	128	4.26	3.98	2.16	2.06	21.75	27.88
$x = 2$ (para-Cl)	2.76	133	4.69	4.07	2.33	2.09	16.97	28.76
$x = 2$ (ortho-Cl)	2.86	137	4.48	4.50	2.25	2.26	18.23	17.97
$x = 3$ (plane-Cl)	2.89	139	5.19	5.54	2.54	2.69	12.58	9.71
$x = 3$ (RT-Cl)	2.98	143	4.68	8.38	2.33	4.15	16.03	1.31
$x = 4$ (para-Br)	2.97	143	5.33	4.95	2.60	2.44	11.37	15.22
$x = 4$ (ortho-Br)	3.10	149	5.25	4.28	2.56	2.17	11.62	25.56
$x = 5$	3.11	149	5.61	5.22	2.72	2.55	9.71	13.01
$x = 6$	3.35	161	7.10	7.90	3.44	3.88	5.07	3.04

volume of its constituent ions is known as the lattice free volume. Thus, the ratio between the free volume and the total volume denotes the specific free volume. It is known that a large free volume creates ample room for atomic motion, thereby strengthening the interaction between electrons and phonons [100]. Table S7 demonstrates that the specific free volume of $Cs_2AgSbBr_{6-x}Cl_x$ rises as the concentration of Cl increases. As a result, in these systems, electron-phonon coupling similarly increases with the concentration of Cl.

Interestingly, on considering the exclusive interaction of the charge carriers with optical phonons, one can use the Fröhlich parameter α to determine an upper limit of charge carrier mobility by calculating the polaron mobility, which is defined using the Hellwarth polaron model [58] as follows:

$$\mu_p = \frac{(3\sqrt{\pi}e)}{2\pi c\omega_{LO} m^* \alpha} \frac{\sinh(\beta/2)}{\beta^{5/2}} \frac{w^3}{v^3} \frac{1}{K(a,b)}, \tag{9}$$

where $\beta = hc\omega_{LO}/k_B T$, and w and v are the temperature-dependent variational parameters. $K(a, b)$ is a function of β, w, and v (for further details, see the Supplemental Material [72]). The free energy minimization method [58] is used to determine the parameters v and w at room temperature (300 K), which are listed in Table S8 of the Supplemental Material [72]. Finally, the determined upper limits for the charge carrier mobility at room temperature are tabulated in Table V. The calculated values of electron and hole mobility for our investigated HDPs are found to lie in the range of 5.07–28.07 $cm^2\,V^{-1}\,s^{-1}$ and 1.31–28.76 $cm^2\,V^{-1}\,s^{-1}$, respectively, similar to or a little smaller than their Pb-based counterparts. This modest charge carrier mobility is due to the small carrier's effective mass and high dielectric constant. One can also witness the ambipolar characteristics in mixed HDPs and the increase in hole mobility when $x = 1$, 2, 4, and 5. It is found that the electron mobility decreases linearly with an increase in the value of x and follows the relation $\mu_p^e = \{(-3.524 \pm 0.359)x + (25.647 \pm 1.295)\}$, $R = 95.06\%$ (R is the coefficient of determination). On the other hand, the hole mobility shows an oscillating behavior with the increase of x, which is evident due to their change of VBM in the band structures (Fig. 3). One should note that since excitonic temperature (T_{exc}) is quite high for these materials, they will remain in an excitonic state at room temperature, and thus, instead of considering charge carrier interaction with polarons, exciton-polaron interaction should have been considered to estimate exciton mobility, as well. However, such calculations are extremely expensive and beyond the scope of the current work.

In the context of polarons, the effective mass of the electron changes due to its interaction with the lattice vibrations (phonons). A cloud of lattice vibrations surrounds the electron, which essentially increases its mass and alters its mobility. Thus, the effective mass of the polaron also influences the carrier-lattice interaction. The effective mass of the polaron (m_p) is defined using Feynman's extended version of Fröhlich's polaron theory as follows [101]:

$$m_p = m^*\left(1 + \frac{\alpha}{6} + \frac{\alpha^2}{40} + \ldots\right), \tag{10}$$

where m^* is the effective mass determined via band structure calculations. The calculated polaron mass of $Cs_2AgSbBr_{6-x}Cl_x$ compounds is tabulated in Table V. We discovered that the polaronic masses of pure and mixed halide perovskites are 2–3 (2–4) times greater than an electron's (hole's) effective masses, confirming the enhanced carrier-lattice interactions, and thereby explaining the relatively lower charge carrier mobility as compared to nonpolar or less-polar perovskites. In any case, the investigated materials are found to exhibit reasonably modest charge carrier mobilities with ambipolar characteristics and desirable stability and nontoxicity, making them a promising class of materials for optoelectronic devices.

IV. CONCLUSIONS

In this paper, we have carried out an extensive study to investigate the suitability of $Cs_2AgSbBr_{6-x}Cl_x$ ($x = 0$, 1, 2, 3, 4, 5, 6) mixed halide double perovskites for optoelectronic devices by calculating their structural, mechanical, electronic, optical, excitonic, and polaronic properties using state-of-the-art ground- and excited-state methods. First, the structures with different halide configurations were modeled and relaxed. The relaxed structures are found to satisfy all

crystallographic stability criteria and are also shown to exhibit structural, thermodynamical, and mechanical stability, hinting at the high possibility of their synthesizability. Further, the investigation of the mechanical properties of these materials reveals them to be flexible and ductile. Focusing on the optoelectronic properties, it is found that the electronic properties calculated using DFT-HSE06 and *GW*-based approaches predict an indirect band gap that varies linearly with x in $Cs_2AgSbBr_{6-x}Cl_x$ and lies in the range of 1.68–2.49 eV. Consequently, by resolving the Bethe-Salpeter equation (BSE), the optical properties are precisely estimated, and the mixed halides $Cs_2AgSbBr_{6-x}Cl_x$ are demonstrated to exhibit absorption in the range of the mid-visible to near-UV spectrum, high absorption coefficient, high exciton binding energy, and longer intrinsic exciton lifetimes. The calculations of transport properties are performed considering electron/hole-phonon interactions as explained by the Fröhlich model, which is not negligible in such materials. The Hellwarth polaron model predicts the electron and hole mobility for our investigated HDPs to lie in the range of 5.07–28.07 $cm^2\,V^{-1}\,s^{-1}$ and 1.31–28.76 $cm^2\,V^{-1}\,s^{-1}$, respectively. Overall, the fundamental understanding developed from this study elucidates mixed halide $Cs_2AgSbBr_{6-x}Cl_x$ perovskites to be a promising class of stable and nontoxic materials for the next-generation flexible optoelectronic devices due to their favorable as well as tunable properties which are not so poor as compared to their hybrid lead perovskite counterpart and are better than their neighboring HDPs.

ACKNOWLEDGMENTS

The high performance computing facility "Magus" and workstations available at the School of Natural Sciences, Shiv Nadar Institution of Eminence, were used to perform all calculations. S.A. would like to acknowledge the Council of Scientific and Industrial Research (CSIR), Government of India [Grant No. 09/1128(11453)/2021-EMR-I], for financial support. S.A. would like to acknowledge Dr. Raja Sen of Laboratoire des Solides Irradiés, Department of Physics, École Polytechnique, for teaching the dynamical stability and HSE06 calculations and for his valuable suggestions. S.A. would also like to acknowledge Dr. Santosh Kumar, Associate Professor at Department of Physics, Shiv Nadar Institution of Eminence, and Dr. Dip Das of Department of Electronic and Electrical Engineering, University College London, for their help in performing the polaron mobility calculations and for providing their valuable suggestions.

[1] Y. Dong, R. Zhu, and Y. Jia, J. Phys. Chem. C **125**, 14883 (2021).
[2] W.-J. Yin, T. Shi, and Y. Yan, Adv. Mater. **26**, 4653 (2014).
[3] S. De Wolf, J. Holovsky, S.-J. Moon, P. Löper, B. Niesen, M. Ledinsky, F.-J. Haug, J.-H. Yum, and C. Ballif, J. Phys. Chem. Lett. **5**, 1035 (2014).
[4] A. Miyata, A. Mitioglu, P. Plochocka, O. Portugall, J. T.-W. Wang, S. D. Stranks, H. J. Snaith, and R. J. Nicholas, Nat. Phys. **11**, 582 (2015).
[5] V. D'Innocenzo, G. Grancini, M. J. P. Alcocer, A. R. S. Kandada, S. D. Stranks, M. M. Lee, G. Lanzani, H. J. Snaith, and A. Petrozza, Nat. Commun. **5**, 3586 (2014).
[6] C. C. Stoumpos, C. D. Malliakas, and M. G. Kanatzidis, Inorg. Chem. **52**, 9019 (2013).
[7] A. R. B. Mohd Yusoff, P. Gao, and M. K. Nazeeruddin, Coord. Chem. Rev. **373**, 258 (2018).
[8] Q. A. Akkerman, G. Rainò, M. V. Kovalenko, and L. Manna, Nat. Mater. **17**, 394 (2018).
[9] G. Giorgi, J.-I. Fujisawa, H. Segawa, and K. Yamashita, J. Phys. Chem. C **118**, 12176 (2014).
[10] M. Anaya, G. Lozano, M. E. Calvo, W. Zhang, M. B. Johnston, H. J. Snaith, and H. Míguez, J. Phys. Chem. Lett. **6**, 48 (2015).
[11] X. Qin, H. Dong, and W. Hu, Sci. China Mater. **58**, 186 (2015).
[12] Q. Lin, A. Armin, P. L. Burn, and P. Meredith, Laser Photon. Rev. **10**, 1047 (2016).
[13] M. Ahmadi, T. Wu, and B. Hu, Adv. Mater. **29**, 1605242 (2017).
[14] A. Kojima, K. Teshima, Y. Shirai, and T. Miyasaka, J. Am. Chem. Soc. **131**, 6050 (2009).
[15] National Renewable Energy Laboratory, Photovoltaic Research, https://www.nrel.gov/pv/cell-efficiency.html.
[16] F. Zhang, B. Yang, Y. Li, W. Deng, and R. He, J. Mater. Chem. C **5**, 8431 (2017).
[17] W. Wang, J. Su, L. Zhang, Y. Lei, D. Wang, D. Lu, and Y. Bai, CrystEngComm **20**, 1635 (2018).
[18] J. H. Noh, S. H. Im, J. H. Heo, T. N. Mandal, and S. I. Seok, Nano Lett. **13**, 1764 (2013).
[19] B. Suarez, V. Gonzalez-Pedro, T. S. Ripolles, R. S. Sanchez, L. Otero, and I. Mora-Sero, J. Phys. Chem. Lett. **5**, 1628 (2014).
[20] E. Edri, S. Kirmayer, M. Kulbak, G. Hodes, and D. Cahen, J. Phys. Chem. Lett. **5**, 429 (2014).
[21] A. Babayigit, A. Ethirajan, M. Muller, and B. Conings, Nat. Mater. **15**, 247 (2016).
[22] B. Zhao, S. Bai, V. Kim, R. Lamboll, R. Shivanna, F. Auras, J. M. Richter, L. Yang, L. Dai, M. Alsari, X.-J. She, L. Liang, J. Zhang, S. Lilliu, P. Gao, H. J. Snaith, J. Wang, N. C. Greenham, R. H. Friend, and D. Di, Nat. Photon. **12**, 783 (2018).
[23] S. Xiang, Z. Fu, W. Li, Y. Wei, J. Liu, H. Liu, L. Zhu, R. Zhang, and H. Chen, ACS Energy Lett. **3**, 1824 (2018).
[24] G. Volonakis, M. R. Filip, A. A. Haghighirad, N. Sakai, B. Wenger, H. J. Snaith, and F. Giustino, J. Phys. Chem. Lett. **7**, 1254 (2016).
[25] C. N. Savory, A. Walsh, and D. O. Scanlon, ACS Energy Lett. **1**, 949 (2016).
[26] S. Adhikari and P. Johari, Phys. Rev. Mater. **7**, 075401 (2023).
[27] W. Deng, Z.-Y. Deng, J. He, M. Wang, Z.-X. Chen, S.-H. Wei, and H.-J. Feng, Appl. Phys. Lett. **111**, 151602 (2017).
[28] F. Wei, Z. Deng, S. Sun, N. T. P. Hartono, H. L. Seng, T. Buonassisi, P. D. Bristowe, and A. K. Cheetham, Chem. Commun. **55**, 3721 (2019).
[29] J. C. Dahl, W. T. Osowiecki, Y. Cai, J. K. Swabeck, Y. Bekenstein, M. Asta, E. M. Chan, and A. P. Alivisatos, Chem. Mater. **31**, 3134 (2019).

[30] J. E. F. S. Rodrigues, C. A. Escanhoela, B. Fragoso, G. Sombrio, M. M. Ferrer, C. Álvarez-Galván, M. T. Fernández-Díaz, J. A. Souza, F. F. Ferreira, C. Pecharromán, and J. A. Alonso, Ind. Eng. Chem. Res. **60**, 18918 (2021).

[31] T. T. Tran, J. R. Panella, J. R. Chamorro, J. R. Morey, and T. M. McQueen, Mater. Horiz. **4**, 688 (2017).

[32] E. Greul, M. L. Petrus, A. Binek, P. Docampo, and T. Bein, J. Mater. Chem. A **5**, 19972 (2017).

[33] A. C. Dakshinamurthy, M. Gupta, B. R. K. Nanda, and C. Sudakar, J. Phys. Chem. C **127**, 1588 (2023).

[34] H. Chen, S. Ming, M. Li, B. Wang, and J. Su, J. Phys. Chem. C **125**, 11271 (2021).

[35] J. Su, T. Mou, J. Wen, and B. Wang, J. Phys. Chem. C **124**, 5371 (2020).

[36] K.-z. Du, W. Meng, X. Wang, Y. Yan, and D. B. Mitzi, Angew. Chem. Int. Ed. **56**, 8158 (2017).

[37] D. Han, M. Ogura, A. Held, and H. Ebert, ACS Appl. Mater. Interfaces **12**, 37100 (2020).

[38] M. Jain, P. Bhumla, M. Kumar, and S. Bhattacharya, J. Phys. Chem. C **126**, 6753 (2022).

[39] M. Kumar Chini, S. Goverapet Srinivasan, N. K. Tailor, Yukta, D. Salahub, and S. Satapathi, Chem. Phys. **529**, 110547 (2020).

[40] M. B. Gray, E. T. McClure, and P. M. Woodward, J. Mater. Chem. C **7**, 9686 (2019).

[41] H. Wu, A. Erbing, M. B. Johansson, J. Wang, C. Kamal, M. Odelius, and E. M. J. Johansson, ChemSusChem **14**, 4507 (2021).

[42] Y. Liang, J. Alloys Compd. **862**, 158575 (2021).

[43] T. Atsue, I. Ogunniranye, and O. Oyewande, Mater. Sci. Semicond. Process. **133**, 105963 (2021).

[44] J. Breternitz, S. Levcenko, H. Hempel, G. Gurieva, A. Franz, A. Hoser, and S. Schorr, J. Phys. Energy **1**, 025003 (2019).

[45] X.-G. Zhao, J.-H. Yang, Y. Fu, D. Yang, Q. Xu, L. Yu, S.-H. Wei, and L. Zhang, J. Am. Chem. Soc. **139**, 2630 (2017).

[46] H. Shi and M.-H. Du, Phys. Rev. Appl. **3**, 054005 (2015).

[47] S. Saikia, A. Joshi, H. Arfin, S. Badola, S. Saha, and A. Nag, Angew. Chem. Int. Ed. **61**, e202201628 (2022).

[48] J. Zhou, X. Rong, M. S. Molokeev, X. Zhang, and Z. Xia, J. Mater. Chem. A **6**, 2346 (2018).

[49] M. R. Filip, J. B. Haber, and J. B. Neaton, Phys. Rev. Lett. **127**, 067401 (2021).

[50] P. Hohenberg and W. Kohn, Phys. Rev. **136**, B864 (1964).

[51] W. Kohn and L. J. Sham, Phys. Rev. **140**, A1133 (1965).

[52] S. Albrecht, L. Reining, R. Del Sole, and G. Onida, Phys. Rev. Lett. **80**, 4510 (1998).

[53] M. Rohlfing and S. G. Louie, Phys. Rev. Lett. **81**, 2312 (1998).

[54] L. Hedin, Phys. Rev. **139**, A796 (1965).

[55] M. S. Hybertsen and S. G. Louie, Phys. Rev. Lett. **55**, 1418 (1985).

[56] J. Heyd, G. E. Scuseria, and M. Ernzerhof, J. Chem. Phys. **118**, 8207 (2003).

[57] R. Kentsch, M. Scholz, J. Horn, D. Schlettwein, K. Oum, and T. Lenzer, J. Phys. Chem. C **122**, 25940 (2018).

[58] R. W. Hellwarth and I. Biaggio, Phys. Rev. B **60**, 299 (1999).

[59] G. Kresse and J. Furthmüller, Phys. Rev. B **54**, 11169 (1996).

[60] G. Kresse and J. Furthmüller, Comput. Mater. Sci. **6**, 15 (1996).

[61] P. E. Blöchl, Phys. Rev. B **50**, 17953 (1994).

[62] J. P. Perdew, K. Burke, and M. Ernzerhof, Phys. Rev. Lett. **77**, 3865 (1996).

[63] K. Momma and F. Izumi, J. Appl. Crystallogr. **44**, 1272 (2011).

[64] A. M. Ganose, A. J. Jackson, and D. O. Scanlon, J. Open Source Softw. **3**, 717 (2018).

[65] M. Gajdoš, K. Hummer, G. Kresse, J. Furthmüller, and F. Bechstedt, Phys. Rev. B **73**, 045112 (2006).

[66] J. Xu, J.-B. Liu, J. Wang, B.-X. Liu, and B. Huang, Adv. Funct. Mater. **28**, 1800332 (2018).

[67] C. Li, X. Lu, W. Ding, L. Feng, Y. Gao, and Z. Guo, Acta Crystallogr. B **64**, 702 (2008).

[68] G. Volonakis, A. A. Haghighirad, R. L. Milot, W. H. Sio, M. R. Filip, B. Wenger, M. B. Johnston, L. M. Herz, H. J. Snaith, and F. Giustino, J. Phys. Chem. Lett. **8**, 772 (2017).

[69] C. J. Bartel, C. Sutton, B. R. Goldsmith, R. Ouyang, C. B. Musgrave, L. M. Ghiringhelli, and M. Scheffler, Sci. Adv. **5**, eaav0693 (2019).

[70] G. Kieslich, S. Sun, and A. K. Cheetham, Chem. Sci. **6**, 3430 (2015).

[71] Z. Li, S. R. Kavanagh, M. Napari, R. G. Palgrave, M. Abdi-Jalebi, Z. Andaji-Garmaroudi, D. W. Davies, M. Laitinen, J. Julin, M. A. Isaacs, R. H. Friend, D. O. Scanlon, A. Walsh, and R. L. Z. Hoye, J. Mater. Chem. A **8**, 21780 (2020).

[72] See Supplemental Material at http://link.aps.org/supplemental/10.1103/PhysRevB.110.014101 for the details of crystal structures, bond lengths, dynamical and mechanical stability, Bader charge analysis, total and partial density of states using HSE06, details of the effective masses, number of occupied (NO) and unoccupied (NV) bands, and NBANDS for the convergence of BSE calculation, real and imaginary part of electronic dielectric function using the BSE@G_0W_0@PBE method, strength of electron-phonon coupling, determination of single phonon angular frequency and the Debye temperature, and parameters for calculating the polaron mobility of $Cs_2AgSbBr_{6-x}Cl_x$ compounds. It also contains Refs. [102–104].

[73] X. Ye, A. Liu, Y. Zhao, Q. Han, T. Kitamura, and T. Ma, Int. J. Energy Res. **46**, 8471 (2022).

[74] Q. Mahmood, M. Younas, M. G. B. Ashiq, S. M. Ramay, A. Mahmood, and H. M. Ghaithan, Int. J. Energy Res. **45**, 14995 (2021).

[75] V. Mithal, S. Adhikari, and P. Johari, Adv. Theory Simul. **6**, 2200694 (2023).

[76] F. Mouhat and F.-X. Coudert, Phys. Rev. B **90**, 224104 (2014).

[77] Z.-j. Wu, E.-j. Zhao, H.-p. Xiang, X.-f. Hao, X.-j. Liu, and J. Meng, Phys. Rev. B **76**, 054115 (2007).

[78] Q.-J. Liu, Z.-T. Liu, and L.-P. Feng, Phys. Status Solidi B **248**, 1629 (2011).

[79] R. Hill, Proc. Phys. Soc. A **65**, 349 (1952).

[80] S. Pugh, London, Edinburgh, Dublin Philos. Mag. J. Sci. **45**, 823 (1954).

[81] K.-q. Wang, Y. He, M. Zhang, J.-j. Shi, and W.-w. Cai, J. Phys. Chem. C **125**, 21160 (2021).

[82] S. Saha, T. P. Sinha, and A. Mookerjee, Phys. Rev. B **62**, 8828 (2000).

[83] M. Jain, J. R. Chelikowsky, and S. G. Louie, Phys. Rev. Lett. **107**, 216806 (2011).

[84] P. Basera, A. Singh, D. Gill, and S. Bhattacharya, J. Mater. Chem. C **9**, 17113 (2021).

[85] X. Liu, B. Xie, C. Duan, Z. Wang, B. Fan, K. Zhang, B. Lin, F. J. M. Colberts, W. Ma, R. A. J. Janssen, F. Huang, and Y. Cao, J. Mater. Chem. A **6**, 395 (2018).
[86] M. Kumar, A. Singh, D. Gill, and S. Bhattacharya, J. Phys. Chem. Lett. **12**, 5301 (2021).
[87] X. Wang, W. Meng, and Y. Yan, J. Appl. Phys. **122**, 085104 (2017).
[88] F. Ferreira, A. J. Chaves, N. M. R. Peres, and R. M. Ribeiro, J. Opt. Soc. Am. B **36**, 674 (2019).
[89] R.-I. Biega, M. R. Filip, L. Leppert, and J. B. Neaton, J. Phys. Chem. Lett. **12**, 2057 (2021).
[90] K. R. Hansen, J. S. Colton, and L. Whittaker-Brooks, Adv. Opt. Mater. **12**, 2301659 (2024).
[91] M. Jain, D. Gill, P. Bhumla, P. Basera, and S. Bhattacharya, Appl. Phys. Lett. **118**, 192103 (2021).
[92] S. Adhikari and P. Johari, Phys. Rev. B **109**, 174114 (2024).
[93] M. Bokdam, T. Sander, A. Stroppa, S. Picozzi, D. D. Sarma, C. Franchini, and G. Kresse, Sci. Rep. **6**, 28618 (2016).
[94] C. D. Spataru and F. Leonard, Chem. Phys. **413**, 81 (2013).
[95] M. Bonn, K. Miyata, E. Hendry, and X.-Y. Zhu, ACS Energy Lett. **2**, 2555 (2017).
[96] L.-K. Gao and Y.-L. Tang, ACS Omega **6**, 11545 (2021).
[97] L. M. Herz, ACS Energy Lett. **2**, 1539 (2017).
[98] J. M. Frost, Phys. Rev. B **96**, 195202 (2017).
[99] H. Fröhlich, Adv. Phys. **3**, 325 (1954).
[100] J. He, W.-H. Fang, and R. Long, J. Phys. Chem. Lett. **9**, 4834 (2018).
[101] R. P. Feynman, Phys. Rev. **97**, 660 (1955).
[102] J. Even, L. Pedesseau, C. Katan, M. Kepenekian, J.-S. Lauret, D. Sapori, and E. Deleporte, J. Phys. Chem. C **119**, 10161 (2015).
[103] K. Ohara, T. Yamada, H. Tahara, T. Aharen, H. Hirori, H. Suzuura, and Y. Kanemitsu, Phys. Rev. Mater. **3**, 111601(R) (2019).
[104] C. D. Spataru, S. Ismail-Beigi, R. B. Capaz, and S. G. Louie, Phys. Rev. Lett. **95**, 247402 (2005).